

Article

High Cycle Fatigue Performance of Inconel 718 Alloys with Different Strengths at Room Temperature

Liqiong Zhong^{1,2,3}, Hao Hu³, Yilong Liang^{2,4,5,*} and Chaowen Huang^{2,4,5}¹ College of Mechanical Engineering, Guizhou University, Guiyang 550025, China; zhenyuan04@163.com² College of Materials and Metallurgy, Guizhou University, Guiyang 550025, China; cw Huang@gzu.edu.cn³ College of Mechanical Engineering, Guizhou University, Guiyang 550005, China; huhao105@126.com⁴ Guizhou Key Laboratory of Materials Strength and Structure, Guiyang 550025, China⁵ High Performance Metal Structure Material and Manufacture Technology National Local Joint Engineering Laboratory, Guiyang 550025, China

* Correspondence: liangyilong@126.com; Tel.: +86-130-3782-6595

Received: 21 November 2018; Accepted: 18 December 2018; Published: 21 December 2018



Abstract: In this paper, the high cycle fatigue performance of solid solution state and aged Inconel 718 superalloys was studied at room temperature. Scanning electron microscopy (SEM) and transmission electron microscopy (TEM) were used to analyze the original structural features and fatigue deformation features of two kinds of alloys. SEM, laser scanning confocal microscopy, and electron backscatter diffraction (EBSD) were used to analyze the secondary fracture features of the fatigue fracture morphology and fatigue fracture profile. The results showed that the aging treatment significantly affected the strength and plasticity of the alloy, which in turn affected the fatigue performance of the alloy. After the aging treatment, the yield strength σ_s and the tensile strength σ_b of the Inconel 718 alloy increased by 152% and 65.9%, respectively, compared with those of the solid solution state, but the rate of elongation δ and rate of contraction in the cross-section area φ decreased by 63.7% and 52.3%, respectively. The fatigue limit of the aged state was lower than that of the solid solution state by 6.3%. The quadratic function relationship between the high cycle fatigue limit σ_{-1} and the tensile strength σ_b of the Inconel 718 superalloy at room temperature was $\sigma_{-1} = \sigma_b \cdot (0.869 - 3.67 \times 10^{-4} \cdot \sigma_b)$. An analysis of the fatigue fracture mechanism showed that the fatigue fractures before and after aging were all initiated in the grains oriented relatively unfavorably on the surface of the sample, with a mixture of intergranular and transgranular propagation after the transgranular propagation of several grains. The higher plasticity of the solid solution state Inconel 718 alloy resulted in a large number of slip deformation zones under high cycle fatigue loads, and the plastic deformation was relatively uniform. The lengths of the secondary fractures were as high as 120 μm , which formed the single-source plastic fatigue fracture that promoted an increase in the fatigue limit. After aging treatment, the higher strength of the Inconel 718 alloy made dislocation slip difficult under high cycle fatigue loads, and the plasticity compatible deformation capability was poor. When local dislocations slipped to the intragranular γ'' phase, γ' phase, or interfaces with nonmetallic compounds (NMCs), plugging occurred. The degree of stress concentration increased, causing the initiation of fatigue fracture; the secondary fracture was approximately 20 μm . Brittle cleavage due to multiple sources significantly reduced the fatigue limit.

Keywords: Inconel 718 superalloys; room temperature; high cycle fatigue

1. Introduction

The Inconel 718 superalloy (the trademark in China is GH4169) is a nickel-chromium-iron (Ni-Cr-Fe)-based wrought superalloy that is precipitation-hardened and was successfully developed

by the United States in the 1950s [1]. In the aging treatment process, the γ'' phase, which is coherent with the matrix γ phase (Ni_3Nb , body-centered tetragonal DO_{22} structure), and the γ' phase, which is semicoherent with the γ phase (face-centered cubic L1_2 structure), disperses precipitation and hinders dislocation motion, not only giving the Inconel 718 alloy a higher room temperature strength but also allowing this alloy to maintain a comparatively high strength at high temperatures under 650 °C. Thus, this alloy is widely used in the manufacture of turbine discs and blades for aircraft engines and other key parts and components exposed to high temperatures and fasteners not exposed to high temperatures. The high-frequency vibrations of an aircraft engine during operation generate disturbance stress effects on the nearby parts and components, requiring the Inconel 718 alloy to have not only good static strength and creep performance but also good fatigue performance. Therefore, the research on fatigue performance of the Inconel 718 alloy has been widely concerned. According to the specific service environment temperature and load of the parts, it can be roughly divided into several aspects: high temperature [2]/medium temperature [3]/room temperature [4,5] low cycle fatigue, high temperature [6,7]/room temperature [8]/low temperature [9,10] high cycle fatigue, and ultra-high cycle fatigue [11,12] performance. Fournier et al. [13] found that the Inconel 718 alloy in the solution treated and aged (ST + A) state had cyclic softening while in the direct aged (DA) state [14] had cyclic hardening under high temperature. The ST + A state of the Inconel 718 alloy hardens at the initial stage of circulation followed by fatigue softening under room temperature, which is also noted in Inconel 718 alloys with different heat treatment processes [15] and long-term aging [5]. The cyclic deformation mechanisms were studied at different temperatures by Sanders et al. [16] and Xiao et al. [17,18]. As for the relationship between fatigue life and strain amplitude, studies have shown that both ST + A state [19] and DA state [20] Inconel 718 alloys meet the Manson-Coffin relation at high temperatures, while ST + A state [4] alloys and other aged state [15] alloys meet the bilinear Manson-Coffin relation at room temperature. According to the different factors affecting the low-cycle fatigue performance, the influence of microstructure on the low-cycle fatigue life of notch [21] and hot forged alloys [22], the influence of delta phase content [23] and thermal corrosion [24] on low-cycle fatigue behavior, and the influence of frequency and waveform on fatigue crack propagation rate [25] have been studied. Nowadays, the damage tolerance is increasingly applied to turbine blades, Citarella et al. [26,27] have shown that even with a crack, the blade might avoid replacement if accurate propagation of crack could validate such a maintenance choice, and Chang et al. [28] studied the influence of solid-solution temperature on damage tolerance.

The aforementioned studies may consider the reason that aging treatments substantially increase the static strength of the Inconel 718 alloy. The researchers almost always used aged (DA or ST + A) state Inconel 718 alloy with the zigzag curve phenomenon that occurs on the plastic section from the hysteresis loop [29,30] and cyclic softening under high temperature low cycle fatigue; under room temperature low cycle fatigue, the dual-slope Manson-Coffin relationship between the cyclic strain and fatigue life and the softening that occurs immediately following hardening in the initial stage of the cycle are both attributed to γ'' phase shearing in the aged state. However, Rae et al. [31] and Praveen et al. [32] studied the low cycle fatigue characteristics of ST state Inconel 718 alloy at room temperature and found that the ST state was the same as the aged state alloy, as the ST state presented the zigzag curve phenomenon on the plastic section from the hysteresis loop [31] and satisfied the dual-slope Manson-Coffin relationship between the cyclic strain and the cyclic softening and low cycle fatigue life immediately following hardening in the initial stage of the cycle [32]. These results show that, under low cycle fatigue at room temperature, the ST state and the aged state alloys follow the same trends. However, experimental results in the literature [32] also demonstrated that when the total strain amplitude was within the range of 0.625–0.95, the life of the ST state with low strength was higher than that of the ST + A state with high strength. It is regrettable that the author did not explore in detail the reasons behind this phenomenon and simply attributed the phenomenon to the insufficient plasticity of the ST + A state.

Therefore, under low cycle fatigue at room temperature, ST state Inconel 718 alloy has a longer life than that of the ST + A state. It is unknown if this phenomenon is unique to low cycle fatigue or does it also exist for high cycle fatigue, or if the specific reason is an issue that is as yet unsolved. In addition, the specific relationship between the tensile strength σ_b and the fatigue limit σ_{-1} of the Inconel 718 alloy at room temperature remains to be answered. In connection with the aforementioned questions, this paper intends to study the high cycle fatigue behavior of the ST state and the ST + A state Inconel 718 alloys at room temperature and to carry out systematic comparative observations of high cycle fatigue (HCF) fractures. The corresponding relationship between the σ_b and σ_{-1} of the Inconel 718 alloy is fitted according to the test results in anticipation of providing an experimental and theoretical basis for studying the HCF of Inconel 718 alloy at room temperature.

2. Materials and Methods

2.1. Experimental Materials

The material used in this study was the Inconel 718 superalloy with a chemical composition (mass fraction/%) of the following: 0.04 C, 0.22 Mn, 0.009 P, 0.002 S, 0.26 Si, 18.15 Cr, 52.1 Ni, 0.04 Cu, 3.09 Mo, 0.51 Al, 0.92 Ti, 0.09 Co, 4.96 Nb, and 0.005 B, with the remainder as Fe. The ST process was as follows: 980 °C \times 1 h, air cooling. The ST + A process was as follows: 980 °C \times 1 h, air cooling, 720 °C \times 8 h, furnace cooling to 620 °C \times 8 h, air cooling. The original structures of the two states are as shown in Figure 1. Since the solid solution process of the two states was the same, the ST state and the ST + A state did not have obvious differences in terms of average grain size, δ phase and nonmetallic compound (NMC) content, morphology, and distribution, as well as the size, content, and distribution of the annealing twins. The average grain size was approximately 15 μ m, and δ phase and NMCs were present at the grain boundaries and within the grains, which contained certain amounts of annealing twins. Figure 2 shows the transmission electron microscopy (TEM) image of the original structures. The ST state that had not undergone aging treatment had an extremely small amount of γ'' phase precipitation from the process of 980 °C air cooling to room temperature (Figure 2a), and the ST + A state had a large amount of γ'' phase precipitation after standard bipolar aging treatment. The mechanical properties of the ST state and ST + A state Inconel 718 alloys at room temperature are shown in Table 1. The yield strength σ_s and tensile strength σ_b of the ST + A state increased by 152% and 65.9%, respectively, compared with those of the ST state, but the rate of elongation δ and the rate of contraction in the cross-section area φ decreased by 63.7% and 52.3%, respectively.

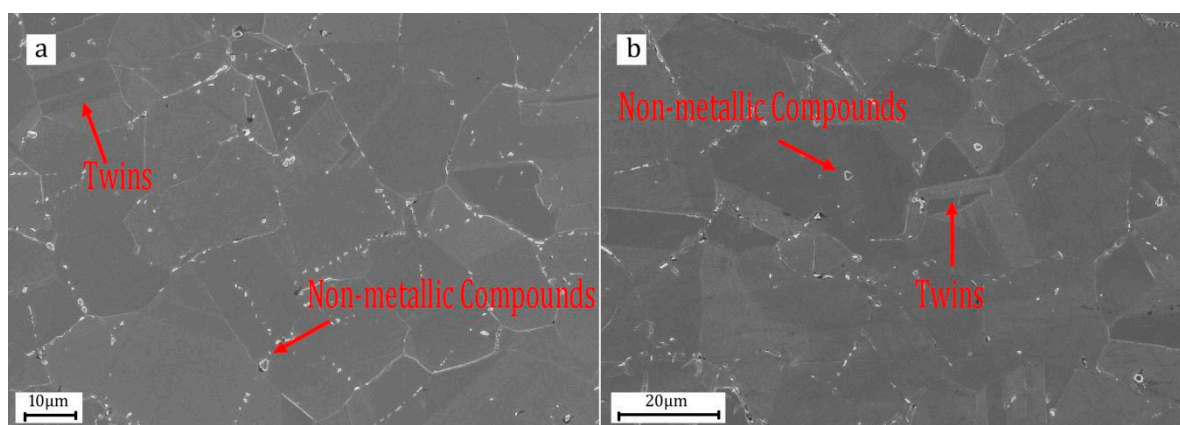


Figure 1. Scanning electron microscopy (SEM) picture of Microstructures. (a) Solution treated (ST) state; (b) solution treated and aged (ST + A) state.

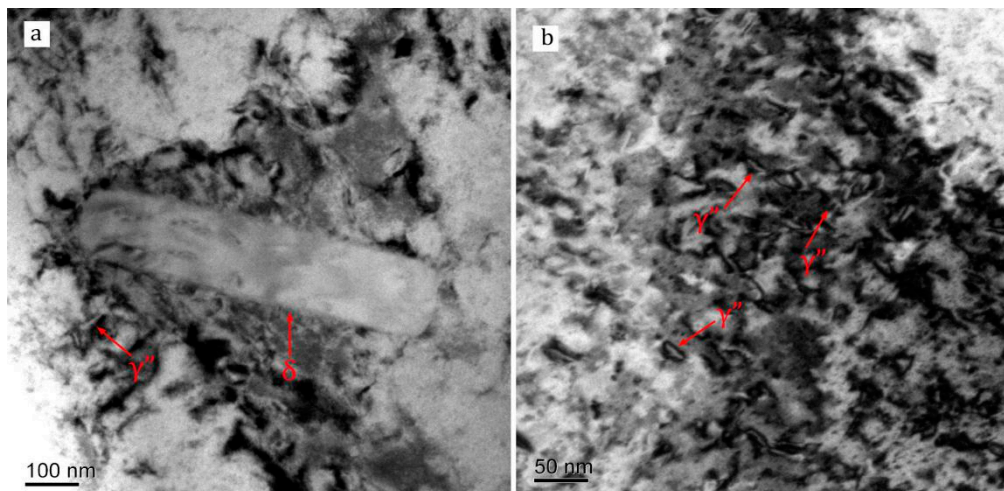


Figure 2. Transmission electron microscopy (TEM) picture of Microstructure, (a) ST state; (b) ST + A state.

Table 1. The mechanical properties of Inconel 718 at room temperature.

State	σ_s /MPa	σ_b /MPa	δ /%	φ /%
ST	528	940	43.5	63.1
ST + A	1332	1560	15.8	30.1

2.2. Experimental Methods

The smooth fatigue sample designed according to GB/T3075-2008 is shown in Figure 3. After the sample was processed, fine sandpaper and polishing cloth were used to manually polish and grind in the axial direction to remove the machining marks perpendicular to the axis. Subsequently, solid solution and aging treatments were carried out separately in a vacuum atmosphere furnace (Hua Wei Company, Heze, China); then, the room temperature HCF tests at 10^7 instances were carried out on the ST + A and ST samples on a QBG-100 high-frequency testing machine (Qian Bang Company, Changchun, China) in air, using the $R = -1$ tension and compression load-control mode; and a frequency of around 130 Hz. The fatigue limit was tested with the up and down method, and the interval stress ($\Delta\sigma$) of the ST + A state and the ST state was 25 and 20 MPa, respectively. The fatigue life of high stress was tested with the group experiment method; three samples were used for each stress level. Finally, the measured data were fitted into a stress vs. number of cycles to failure (S-N) curve.

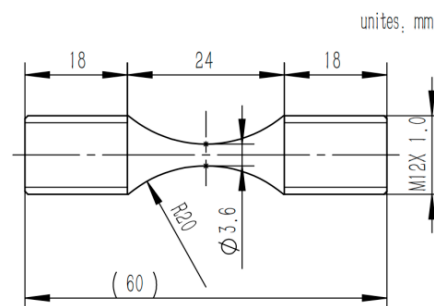


Figure 3. The fatigue specimen of Inconel 718.

First, wire-cutting was used to cut the fatigue fracture from the fatigue fracture sample, and scanning electron microscopy (SEM) (Zeiss, Analytik Jena city, Thuringia, Germany) was used to observe the morphological features of the fatigue fracture. Then, wire-cutting was used again to cut the fatigue fracture that had undergone SEM observation from the fatigue source in the axial direction.

The vertical section of the fatigue fracture was mounted and polished after burnishing with sandpaper. After undergoing chemical etching (5 g CuCl₂, 100 mL HCl, and 100 mL ethanol), laser scanning confocal microscopy (Olympus, Nishi-Shinjuku, Japan) was used to observe the initiation position of the secondary fracture, the length of the secondary fracture, and the propagation mode for the main fracture on the vertical section of the fatigue fracture. The sample from the vertical section of the fatigue fracture observed by laser scanning confocal microscopy was mechanically polished after burnishing again with sandpaper, and the surface was then polished by vibration for approximately 12 h. Next, electron backscatter diffraction (EBSD) (Zeiss, Analytik Jena, Thuringia, Germany) observations were carried out with a scanning step and a range of 0.08 μm and 425 μm × 250 μm, respectively. Channel5 software (Zeiss, Analytik Jena, Thuringia, Germany) was used to analyze the EBSD results. EBSD observation was carried out first on the ST + A state sample, after which observation by laser scanning confocal microscopy was carried out. Wire-cutting was used to cut a thin section of 0.4 mm thickness perpendicular to the axial direction near the fatigue fracture on another section of the fatigue fracture. Sandpaper was used to grind the thin section until the thickness was approximately 50 μm. A small round disc of φ3 was taken from the thin section. Finally, twin-jet thinning was performed on the φ3 small round disc (5 vt % perchloric acid + 95 vt % ethanol) to penetration, and TEM observation was carried out.

3. Results

3.1. High Cycle Fatigue S-N Curve

The high cycle fatigue S-N curve of the Inconel 718 alloy at room temperature is shown in Figure 4. The 10⁷ instances of fatigue limit σ_{-1} could be calculated by Equation (1) [33]:

$$\sigma_{-1} = \frac{1}{m} \sum_{i=1}^n \sigma_i v_i \quad (1)$$

where m is total number of effective specimens, n is the grade of stress amplitude levels, σ_i is the stress amplitude level of i , and v_i is the number of specimens at the stress level of i . Therefore, the σ_{-1} of the ST state and the ST + A state is approximately 492 and 461 MPa, respectively. The fatigue limit of the ST state was higher than that of the ST + A state by 6.73%. Due to the σ_{-1} of the ST state being near to its yield strength σ_s , the stress amplitude of the ST state is equal to or even higher than σ_s , and therefore the fatigue life of the ST + A state was higher than that of the ST state within 10³–10⁵ cycles. In the low stress amplitude zone after 10⁶ instances, the fatigue data of the ST + A state was more dispersed.

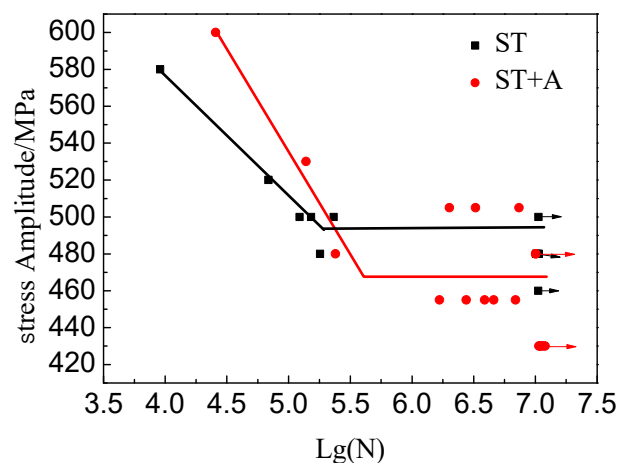


Figure 4. Stress vs. number of cycles to failure (S-N) curve of Inconel 718 at room temperature.

3.2. Fatigue Fracture Morphology

Figure 5 is the diagram of the fatigue fracture morphology for the ST fatigue sample ($\sigma = 480$ MPa, $N = 1.798 \times 10^5$). The macroscopic diagram of the fatigue fracture (Figure 5a) shows that the fatigue fracture of the ST state initiated on the surface with a single fatigue source and a comparatively flat cross-section. The magnified view of the fatigue source in Figure 5b shows that the fatigue source of the ST state has obvious plastic fracture features.

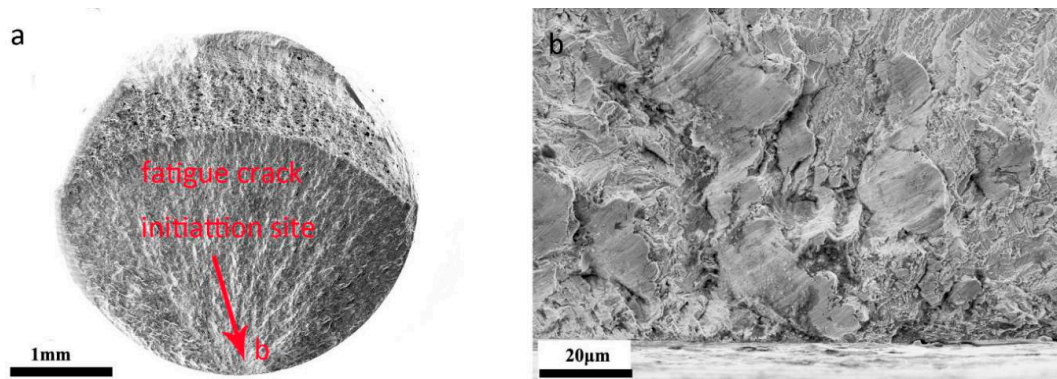


Figure 5. Fatigue fracture surface of ST specimens. (a) Macrograph; (b) local magnification of the fatigue source.

Figure 6 is the diagram of the fatigue fracture morphology for the ST + A fatigue sample ($\sigma = 480$ MPa, $N = 1.765 \times 10^5$). The fatigue sources of the ST + A state are indicated by the arrows in Figure 6a, which show multisource fatigue fracture features similar to the results of Ma et al. [34] and Xie et al. [35]. The fatigue fractures on the plane intersect after undergoing propagation and make the cross-section rougher. The morphology of the cleavage facets for the fatigue source area, as indicated by the arrows in Figure 6b,c, shows brittle cleavage for the fatigue source fracture of the ST + A state. For the fatigue source area in Figure 6c, not only was the NMCs observed, but the NMCs crack was observed as well. The NMC-initiated fatigue crack was observed in Figure 6d.

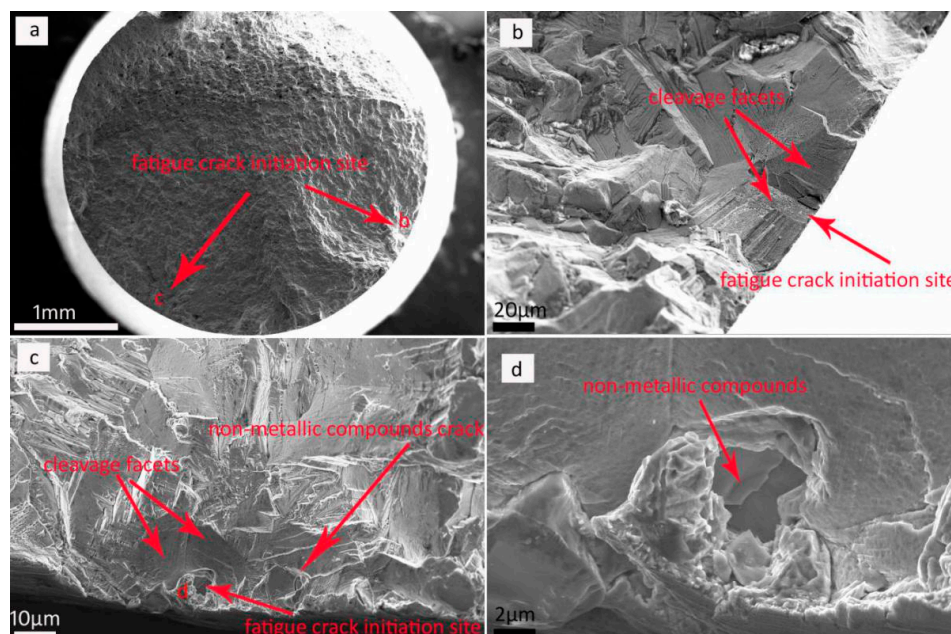


Figure 6. Fatigue fracture surface of ST + A specimens. (a) Macrograph; (b) local magnification of the fatigue source b in (a); (c) local magnification of the fatigue source c in (a); (d) local magnification of the fatigue crack initiation site d in (c).

3.3. Fatigue Fracture Profile

The laser scanning confocal diagrams for the vertical sections of the ST and ST + A fatigue fractures are shown in Figure 7. In Figure 7a, the plane of the ST state fatigue fracture source is 45° to the stress axis, indicating that the fatigue fracture initiated on the $\langle 111 \rangle$ slip plane [34]; this fracture mechanism is different from the room temperature ultrahigh cycle fatigue surface fracture of the aged state Inconel 718 alloy, which initiated at the twin boundaries of the coarse grains [12]. The bumpy morphology of the main fracture shows plastic fracture features. Many plane deformation zones are observed on the fracture profile (Figure 7a,b), which is similar to the low cycle fatigue fracture profile of the aged state at room temperature [13,36]. Three secondary fractures are also observed. In Figure 7a, the length of the secondary fracture for the sample surface grains located near the fatigue source is approximately $20 \mu\text{m}$. In Figure 7b, the lengths of the two secondary fractures for the sample surface grains located directly below the fatigue source are approximately $20 \mu\text{m}$ and $120 \mu\text{m}$. In Figure 7c, the comparatively straight morphology of the main fracture for the ST + A state illustrates brittle fracture features, and no plane deformation zones similar to the ST state were observed in the fracture profile. Two secondary fractures were observed in the interior of the sample. Additionally, in Figure 7c, the length of the secondary fracture located on the main fracture grains is approximately $10 \mu\text{m}$, and a similar secondary fracture was also observed on the high temperature low cycle fatigue fracture profile [2]. In Figure 7d, the length of the fracture located on the NMCs was approximately $5 \mu\text{m}$. In Figure 7c,d, the rectangular frames at the secondary fractures are the traces left on the surface of the sample by the high-voltage electron beam during early EBSD observation.

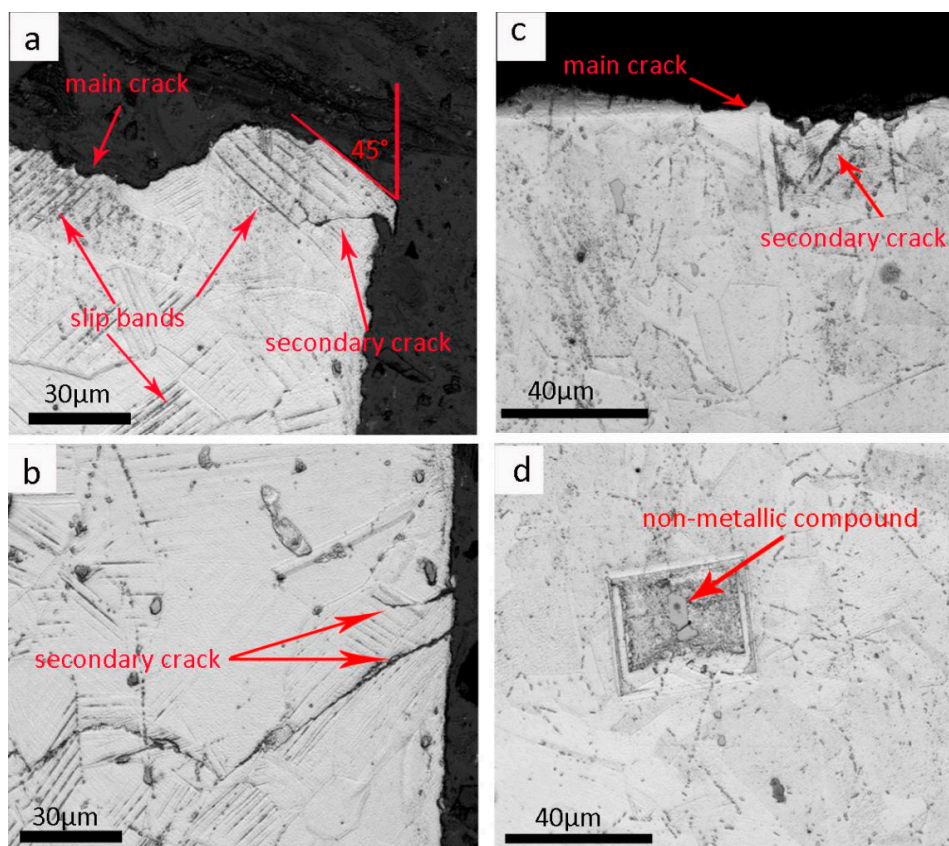


Figure 7. The longitudinal section of the fatigue fracture. (a,b) ST state; (c,d) ST + A state.

3.4. EBSD Observations of the Fatigue Fracture Profile

EBSD observations of the secondary fracture on the fatigue fracture profiles for the ST state and the ST + A state are shown in Figures 8 and 9, respectively. In the Euler graph, yellow is used to

represent the low angle grain boundaries with an orientation difference of less than 15° , red represents the twin boundaries with an orientation difference of approximately 60° , and black represents the high angle grain boundaries. For the ST state fatigue fracture profile in Figure 8a, in addition to the large number of low angle grain boundaries clustered near both the main and secondary fatigue fractures, low angle boundaries also exist in the grains where the fracture is located and on the adjacent grain boundaries. The number of low angle grain boundaries for the ST + A state in Figure 9a is lower than that of the ST state, and these boundaries are mainly aggregated near the main and secondary fatigue fractures and on the grain boundaries, with very few low angle grain boundaries in the interior of the grains. The Schmidt factor (SF) distribution maps of the ST state and ST + A state profiles in Figures 8b and 9b, respectively, show that the SFs of the observed areas are both greater than 0.4, which is favorable for dislocation slip. Secondary fractures initiate in grains with lower average SF, and the secondary fracture of the ST state propagates transgranularly from the grains with low SF toward grains with high SF. The secondary fracture surface of the ST + A state is 45° to the stress axis, and the secondary fracture breaks along the cleavage of the $\langle 111 \rangle$ plane. In Figure 9c, no low angle grain boundaries are aggregated on the two sides of the coarse NMC fracture; the grains adjacent to the NMC have a small number of low angle grain boundaries, and the fracture is straight and shows obvious brittle fracture features. The SF distribution map in Figure 9d shows that the SF of the NMC is different from that of the adjacent grains. The fracture initiates where the size of the transverse section of the coarse NMC is at a minimum, and the fracture is straight with obvious brittle fracture features.

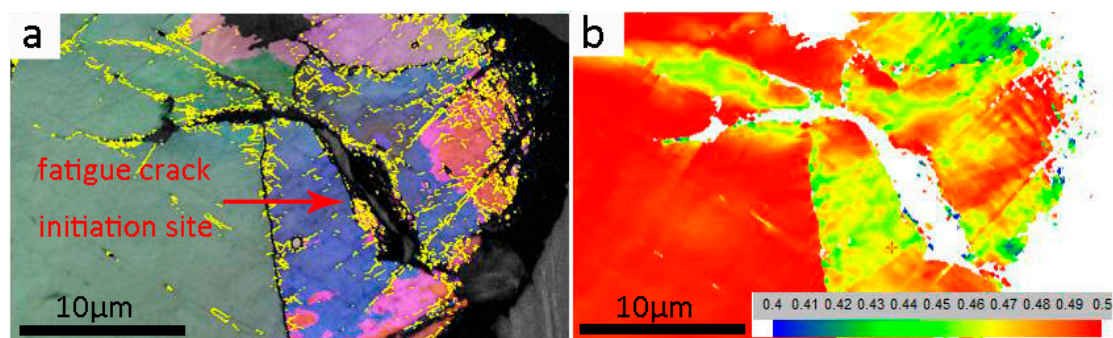


Figure 8. Electron backscatter diffraction (EBSD) picture of ST. (a) The Euler graph; (b) SF distribution.

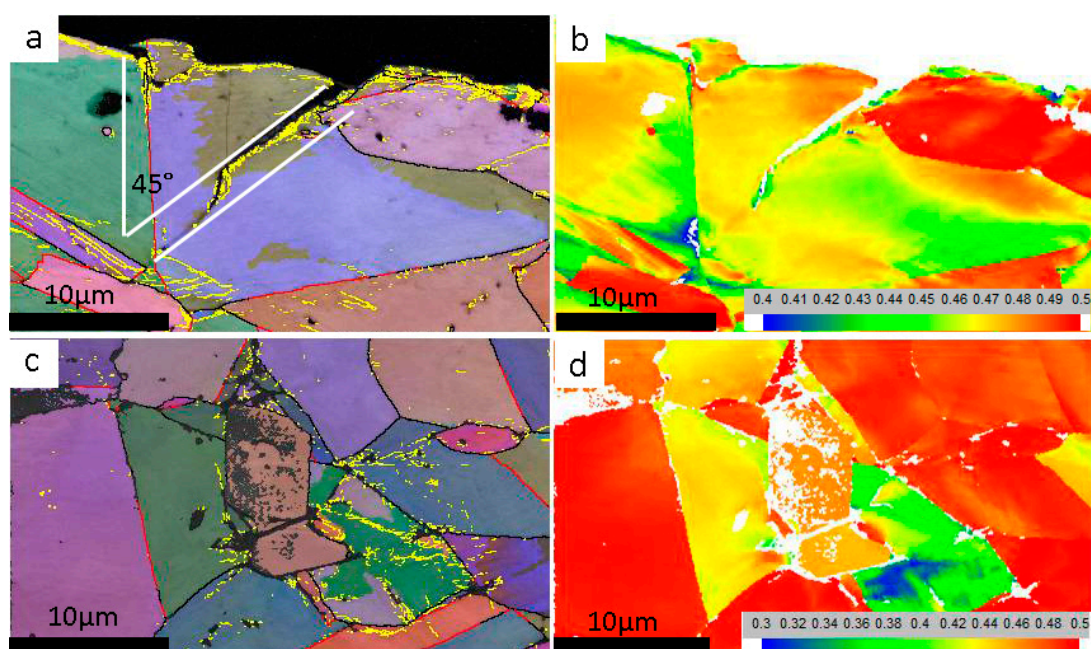


Figure 9. EBSD picture of ST + A. (a,c) The Euler graph; (b,d) SF distribution.

3.5. TEM Observations near the Fatigue Fracture

Figure 10 depicts a TEM image near the fatigue fracture. Compared with the prefatigue TEM image (Figure 2), a large number of dislocations are observed in the TEM images of the fatigue fractures for both states, and the cyclic plastic deformations of the ST state and the ST + A state are both dominated by dislocation slips. The difference is that, due to the good plasticity of the ST state, the dislocations are set into motion simultaneously in multiple slip systems and show multislip plastic deformation features, forming plane slip deformation zones (Figure 7a), and the distribution of the dislocations in the grains is comparatively uniform (Figure 10a). However, for the ST + A state, which has high strength and low plasticity due to the precipitation of the γ'' and γ' phases, the dislocations are hindered by those phases and cannot easily form deformation zones, resulting in the fatigue fracture profile shown in Figure 6a, where deformation zone features are not observed; additionally, the distribution of the dislocations is not as uniform as that of the ST state (Figure 10b).

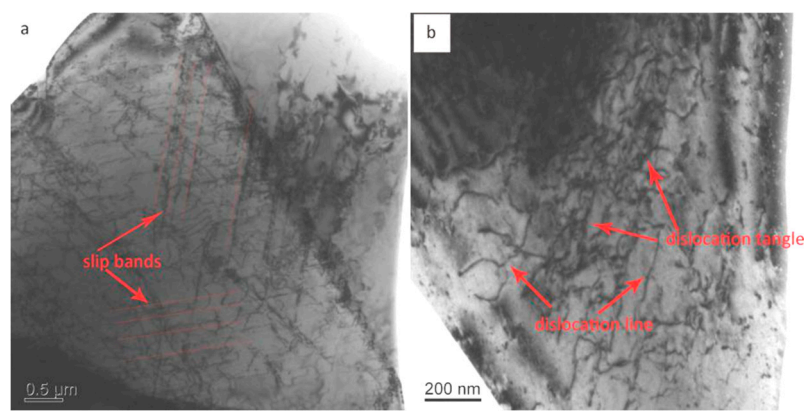


Figure 10. TEM picture of near fatigue source, (a) ST state; (b) ST + A state.

4. Discussion

As shown in the experimental results in Table 1 and Figure 3, at room temperature, the tensile strength σ_b of the Inconel 718 alloy for the ST + A state was much higher than that for the ST state, but the fatigue limit σ_{-1} of the ST + A state was lower than that of the ST state by 31 MPa. This phenomenon is analyzed below from two aspects—the relationship between σ_{-1} and σ_b and the fatigue fracture mechanism.

4.1. Fracture Relationship between the σ_{-1} and σ_b of the Inconel 718 Alloy at Room Temperature

For the precipitation-hardened Inconel 718 superalloy, the increase in σ_b in the ST + A state was due to the precipitation of the precipitation hardening phases and was not caused by a decrease in grain size, a decrease in the NMCs content or size, or a change in twin content. The relationship of $\sigma_{-1} = l \times \sigma_b$, applicable to a fine grain hardening mechanism, could not explain the phenomenon of a ST state with low σ_b but high σ_{-1} . The σ_b in Table 1 and the σ_{-1} calculated according to Figure 3 show that the fatigue to strength ratio of the Inconel 718 alloys with different strengths at room temperature (σ_{-1}/σ_b) was not a fixed constant m ; the fatigue to strength ratios of the ST state and the ST + A state were 0.524 and 0.296, respectively; that is, m decreased as σ_b increased. The study by Pang et al. [37] on metallic materials with a greater range of strengths found that the fatigue to strength ratio m of the material was a linear function of σ_b with a slope of less than 0; that is, $m = c - p \times \sigma_b$, where c and p are coefficients related to the properties of the material. According to $\sigma_{-1} = m \times \sigma_b$, it is easy to infer the following quadratic function for the relationship between σ_{-1} and σ_b :

$$\sigma_{-1} = \sigma_b \times (c - p \times \sigma_b), \quad (2)$$

Equation (2) shows that when $\sigma_b = \frac{c}{2p} \sigma_{-1}$ reaches a maximum value, $\sigma_{-1}^m = \frac{c^2}{4p}$; if σ_b continues to increase, then σ_{-1} decreases; and the σ_b corresponding to σ_{-1}^m is the ideal strength σ_{bc} .

For the Inconel 718 alloy, after respectively substituting the σ_{-1} and σ_b of the ST state and the ST + A state into Equation (2), values of $c = 0.869$ and $p = 3.67 \times 10^{-4}$ were calculated, and the equation in which the σ_{-1} and σ_b of the Inconel 718 alloy at room temperature satisfied the relationship was obtained as:

$$\sigma_{-1} = \sigma_b \cdot (0.869 - 3.67 \times 10^{-4} \cdot \sigma_b), \quad (3)$$

The fatigue limits of the Inconel 718 alloys with different strengths at room temperature were calculated according to Equation (3) and compared with the experimental results for fatigue limits in the literature. The results are shown in Table 2. With the exception of the calculated limit for the axial tensile pull of $R = 0.01$, which differed more from the measured limit, the errors of the rest of the estimations carried out using Equation (3) did not exceed 15%, illustrating that the coefficients c and p calculated from the experimental data in this paper could better reflect the characteristics of the Inconel 718 alloy.

Table 2. The relationship between σ_{-1} and σ_b of inconel 718 alloy at room temperature.

Number	Load Type	Stress Ratio	σ_b /MPa	Experimental σ_{-1} /MPa	Calculated σ_{-1} /MPa	Deviation Rate/%
1	axial	−1	1549	≈420 [38,39]	465	10.7
2	axial	−1	861	≈440 [40]	476	8.2
3	axial	−1	1458	≈440 [9]	486.8	10.6
4	rotating bending	−1	1372	≈450 [41]	501	11.3
5	rotating bending	−1	1390	≈500 [34]	498	0.2
6	rotating bending	−1	1390	≈520 [42]	498	4.2
7	rotating bending	−1	1460	≈460 [43]	486	5.6
8	axial	0.01	1369	≈380 [10]	501	32
9	axial	0.1	1343	≈450 [44]	505	12.25

Equation (3) shows that the Inconel 718 alloy demonstrated $\sigma_{bc} = 1183$ MPa and $\sigma_{-1}^m = 514.4$ MPa. From the characteristics of the quadratic function, when the difference between σ_b and σ_{bc} increases, the corresponding σ_{-1} decreases. After undergoing the aging process treatment described in this paper, the difference between σ_b and σ_{bc} was greater than that in the ST state; therefore, the fatigue limit of the ST + A state was lower than that of the ST state.

4.2. Analysis of the High Cycle Fatigue Fracture of the Inconel 718 Alloy at Room Temperature

From the perspective of the number of fatigue sources, two fatigue sources were observed in the ST + A fatigue fracture (Figure 6a) with $\sigma = 480$ MPa and $N = 1.765 \times 10^5$. Ma et al. [34] and Xie et al. [35] also showed that the high cycle fatigue sources of the aged state Inconel 718 alloy at room temperature had a tendency to change from multisource fatigue to single-source fatigue (after 10^6 instances) as the stress amplitude decreased. Moreover, under the same stress amplitude, the life of the single-source fatigue was longer than that of the multisource fatigue. A single fatigue source was observed in the ST state ($\sigma = 480$ MPa) fatigue fracture (Figure 5a), indicating that the high cycle fatigue performance of the ST state at room temperature was good.

From the perspective of the nucleation features of the fatigue source, the fatigue fracture source of the ST state nucleated by the slipping of the $\langle 111 \rangle$ plane (Figures 3a and 7a), and the two fatigue fracture sources of the ST + A state nucleated by the slipping of the $\langle 111 \rangle$ plane (Figure 4b) and at a coarse NMC (Figure 4c). Pang et al. [37] referred to the defects in the material, such as vacancies, dislocations, stacking faults, and grain boundaries, as the intrinsic defects (IDs) of the material, and they referred to the defects generated in the course of processing the material, such as inclusions and surface scratch marks, as the processing defects (PDs) of the material; these researchers also indicated that the nucleation of fatigue fracture at PDs greatly reduces the fatigue performance. The ST state and

the ST + A state were basically the same in terms of the size and distribution of the NMCs (Figure 1), and the surface treatment process of the fatigue samples was the same; that is, the degree of PD for the two states was the same. Therefore, the ST state fatigue fracture nucleates at IDs, and the ST + A state fatigue fractures nucleate at IDs and PDs, indicating that as the strength of the Inconel 718 alloy increases, the sensitivity of fatigue fracture nucleation at PDs also increases. Under the same stress amplitude, the fatigue fracture sources nucleating at PDs make the fatigue life of the ST + A state lower than that of the ST state.

From the perspective of the fatigue source area as the fracture mode, the ST state had an obvious plastic fracture mode (Figures 5b and 7a), and the small facet of the cleavage for the fatigue fracture area of the ST + A state (Figure 6b,c) illustrated a cleavage fracture mode. Chen et al. [10] showed that the fracture mode of the fatigue source area for an aged state Inconel 718 alloy changed from a transgranular ductile fracture to a cleavage fracture mode as the stress intensity factor k increased at the tip of the fatigue fracture. Accordingly, the k of the fatigue source area of the ST state was inferred to be smaller than that of the ST + A state.

From the perspective of the secondary fracture features of fatigue, the secondary fractures of the ST state were obviously longer than those of the ST + A (Figure 7b–d). Due to the stress intensity factor k at the tip of the secondary crack increasing as the length of the secondary fracture increases, the secondary fracture cannot propagate, which indicates that the larger k , the higher the threshold value Δk_{th} for the propagation of the fatigue fracture, and it is inferred that the Δk_{th} of the ST state is higher than that of the ST + A state. The Δk_{th} of the Inconel 718 superalloy decreased as the strength increases, which is similar to the results of Ritchie et al. [45] regarding 300 M steel. The fracture mode and nucleation source of the secondary fractures on the fatigue fracture profiles of the two states were the same as those of the fatigue source fractures (Figure 7). The average SF of the grains where the secondary fracture source was located was lower than that of the surrounding grains, and the intragranular SF changed more (Figures 8 and 9), which is different from the fatigue surface fracture features observed by Texier et al. [12]. There were more low angle grain boundaries near the secondary fracture of the ST state than that of the ST + A state, and the distribution was more uniform, indicating that the local plastic deformation of the cyclic ST state was more uniform than that of the ST + A state, and the degree of stress concentration was relatively low. This result could also be seen in the TEM images of the fatigue fractures for the two states (Figure 10). Although the cyclic deformation mechanism was the same given that both are dislocation slips, due to the good plasticity of the ST state, dislocations can be set into motion simultaneously in multiple slip systems, and the amount of plastic deformation was large but more uniform, while the amount of plastic deformation for the ST + A state was small but not uniform. Praveen et al. [32] showed that, in regard to the low cycle fatigue of the Inconel 718 alloy at room temperature, the change from uniform plastic deformation under high strain amplitude to nonuniform plastic deformation under low strain amplitude led to the dual-slope Manson-Coffin relationship (the slope of the life-strain curve in the high strain amplitude zone is lower than that in the low strain amplitude zone). This effect may be the reason the fatigue performance of the ST + A state was lower than that of the ST state.

5. Conclusions

- (1) At room temperature, the high cycle fatigue limits (10^7) of the ST state and ST + A state Inconel 718 alloy were 492 MPa and 461 MPa, respectively, and the fatigue limit of the ST state was higher than that of the ST + A state by 6.73%.
- (2) σ_{-1} and σ_b satisfy the quadratic function relationship, $\sigma_{-1} = \sigma_b \cdot (0.869 - 3.67 \times 10^{-4} \cdot \sigma_b)$. First, σ_{-1} increased as σ_b increased; after σ_b exceeded 1183 MPa, σ_{-1} decreased as σ_b increased.
- (3) As σ_b increased, the Inconel 718 alloy changed from single-source plastic fracture to multisource cleavage fracture; the uniform plastic deformation changed to nonuniform plastic deformation.
- (4) The k at the tip of the fatigue source fracture in the ST + A state was larger than that in the ST state, but Δk_{th} was smaller than that in the ST state.

- (5) The secondary fractures on the fatigue fracture profiles of the two states initiated in grains with relatively low SF.
- (6) Conclusions (2), (3), and (4) above are the reasons that the fatigue limit of the ST state is higher than that of the ST + A state.

Author Contributions: Conceptualization, L.Q.Z. and Y.L.L.; methodology, C.W.H.; formal analysis, H.H.; writing—original draft preparation, L.Q.Z.; writing—review and editing, L.Q.Z.; supervision, Y.L.L.

Funding: This research was funded by “The Science and Technology Project of Guizhou Province, grant number (2014) 6012” and “National Natural Science Foundation of China, grant number 51671060”.

Conflicts of Interest: The authors declare no conflict of interest.

References

1. High Temperature Materials Branch of China Metal Institute. In *China Superalloys Handbook*; China Zhijian Publishing House, Standards Press of China: Beijing, China, 2012; p. 645.
2. Hong, B.; Yi, X.; Meng, Q.C. Effect of δ -Ni₃Nb on low cycle fatigue fracture of Inconel 718. *Acta Metall. Sin.* **1991**, *27*, A55–A60.
3. Texier, D.; Gómez, A.C.; Pierret, S.; Franchet, J.M.; Pollock, T.M.; Villechaise, P.; Cormier, J. Microstructural features controlling the variability in low-cycle fatigue properties of alloy Inconel 718DA at intermediate temperature. *Metall. Mater. Trans. A* **2016**, *47*, 1096–1109. [[CrossRef](#)]
4. Bhattacharyya, A.; Sastry, G.V.S.; Kutumbarao, V.V. On the dual slope coffin-manson relationship during low cycle fatigue of Ni-base alloy in 718. *Scr. Mater.* **1997**, *36*, 411–415. [[CrossRef](#)]
5. An, J.L.; Wang, L.; Liu, Y.; Xu, G.; Zhao, G. Influences of long-term aging on microstructure evolution and low cycle fatigue behavior of GH4169. *Acta Metall. Sin.* **2015**, *51*, 835–843.
6. Kobayashi, K.; Yamaguchi, K.; Hayakawa, M.; Kimura, M.; Ogata, T.; Matsuoka, S. High-cycle fatigue properties of alloy 718 for space use. *J. Jpn. Inst. Metals Mater.* **2004**, *68*, 523–525. [[CrossRef](#)]
7. Pradhan, D.; Mahobia, G.S.; Chattopadhyay, K.; Singh, V. Effect of pre hot corrosion on high cycle fatigue behavior of the superalloy IN718 at 600 °C. *Int. J. Fatigue* **2018**, *114*, 120–129. [[CrossRef](#)]
8. Sun, J.; Wang, T.M.; Su, A.P.; Chen, W.Y. Surface integrity and its influence on fatigue life when turning nickel alloy GH4169. *Procedia CIRP* **2018**, *71*, 478–483. [[CrossRef](#)]
9. Ono, Y.; Yuri, T.; Nagashima, N.; Sumiyoshi, H.; Ogata, T.; Nagao, N. High-cycle fatigue properties of alloy 718 base metal and electron beam welded joint. *Phys. Procedia* **2015**, *67*, 1028–1035. [[CrossRef](#)]
10. Ono, Y.; Yuri, T.; Sumiyoshi, H.; Takeuchi, E.; Matsuoka, S.; Ogata, T. High-cycle fatigue properties at cryogenic temperatures in Inconel 718 nickel-based superalloy. *Mater. Trans.* **2004**, *45*, 342–345. [[CrossRef](#)]
11. Yan, N.; Kawagoishi, N.; Chen, Q.; Wang, Q.Y.; Nisitani, H.; Kondo, E. Fatigue properties of Inconel 718 in long life region at elevated temperature. *Key Eng. Mater.* **2003**, *243*, 321–326. [[CrossRef](#)]
12. Texier, D.; Cormier, J.; Villechaise, P.; Stinville, J.C.; Torbet, C.J.; Pierret, S.; Pollock, T.M. Crack initiation sensitivity of wrought direct aged alloy 718 in the very high cycle fatigue regime: The role of non-metallic inclusions. *Mater. Sci. Eng. A* **2016**, *678*, 122–136. [[CrossRef](#)]
13. Fournier, D.; Pineau, A. Low cycle fatigue behavior of Inconel 718 at 298 K and 823 K. *Metall. Trans. A* **1977**, *8*, 1095–1105. [[CrossRef](#)]
14. Xu, J.; Huang, Z.; Jiang, L. Effect of heat treatment on low cycle fatigue of IN718 superalloy at the elevated temperatures. *Mater. Sci. Eng. A* **2017**, *690*, 137–145. [[CrossRef](#)]
15. Praveen, K.V.U.; Singh, V. Effect of heat treatment on coffin-manson relationship in LCF of superalloy IN718. *Mater. Sci. Eng. A* **2008**, *485*, 352–358. [[CrossRef](#)]
16. Sanders, T.H.; Frishmuth, R.E.; Embley, G.T. Temperature dependent deformation mechanisms of alloy 718 in low cycle fatigue. *Metall. Trans. A* **1981**, *12*, 1003–1004. [[CrossRef](#)]
17. Xiao, L.; Chen, D.L.; Chaturvedi, M.C. Shearing of Γ'' precipitates and formation of planar slip bands in Inconel 718 during cyclic deformation. *Scr. Mater.* **2005**, *52*, 603–607. [[CrossRef](#)]
18. Xiao, L.; Chen, D.L.; Chaturvedi, M.C. Cyclic deformation mechanisms of precipitation-hardened Inconel 718 superalloy. *Mater. Sci. Eng. A* **2008**, *483*, 369–372. [[CrossRef](#)]
19. Worthem, D.; Robertson, I.; Leckie, F.; Socie, D.F.; Altstetter, C.J. Inhomogeneous deformation in Inconel 718 during monotonic and cyclic loadings. *Metall. Trans. A* **1990**, *21*, 3215–3220. [[CrossRef](#)]

20. Warren, J.; Wei, D.Y. The cyclic fatigue behavior of direct age 718 at 149, 315, 454 and 538 °C. *Mater. Sci. Eng. A* **2006**, *428*, 106–115. [[CrossRef](#)]
21. Bhowal, P.R.; Wusatowska-Sarnek, A.M. Carbides and their influence on notched low cycle fatigue behavior of fine-grained IN718 gas turbine disk material. *Miner. Metals Mater. Soc.* **2005**, 341–349.
22. Maderbacher, H.; Oberwinkler, B.; Gänser, H.P.; Tan, W.; Rollett, M.; Stoschka, M. The influence of microstructure and operating temperature on the fatigue endurance of hot forged Inconel® 718 components. *Mater. Sci. Eng. A* **2013**, *585*, 123–131. [[CrossRef](#)]
23. Zhang, X.C.; Li, H.C.; Zeng, X.; Tu, S.T.; Zhang, C.C.; Wang, Q.Q. Fatigue behavior and bilinear Coffin-Manson plots of Ni-based GH4169 alloy with different volume fractions of δ phase. *Mater. Sci. Eng. A* **2017**, *682*, 12–22. [[CrossRef](#)]
24. Mahobia, G.S.; Paulose, N.; Mannan, S.L.; Sudhakar, R.G.; Chattopadhyay, K.; Srinivas, N.S.; Singh, V. Effect of hot corrosion on low cycle fatigue behavior of superalloy IN718. *Int. J. Fatigue* **2014**, *59*, 272–281. [[CrossRef](#)]
25. Clavel, M.; Pineau, A. Frequency and wave-form effects on the fatigue crack growth behavior of alloy 718 at 298K and 823K. *Metall. Trans. A* **1978**, *9A*, 471–480. [[CrossRef](#)]
26. Citarella, R.; Giannella, V.; Vivo, E.; Mazzeo, M. FEM-DBEM approach for crack propagation in a low pressure aeroengine turbine vane segment. *Theor. Appl. Fract. Mech.* **2016**, *86*, 143–152. [[CrossRef](#)]
27. Citarella, R.; Giannella, V.; Vivo, E.; Mazzeo, M. Failure analysis for a low pressure aeroengine turbine vane. *Open Mech. Eng. J.* **2017**, *11*, 1–13. [[CrossRef](#)]
28. Chang, M.; Koul, A.K.; Au, P.; Terada, T. Damage tolerance of wrought alloy 718 Ni-Fe-base superalloy. *J. Mater. Eng. Perform.* **1994**, *3*, 356–366. [[CrossRef](#)]
29. Prasad, K.; Sarkar, R.; Ghosal, P.; Kumar, V.; Sundararaman, M. High temperature low cycle fatigue deformation behaviour of forged IN 718 superalloy turbine disc. *Mater. Sci. Eng. A* **2013**, *568*, 239–245. [[CrossRef](#)]
30. Chen, W.; Chaturvedi, M.C. On the mechanism of serrated deformation in aged Inconel 718. *Mater. Sci. Eng. A* **1997**, *229*, 163–168. [[CrossRef](#)]
31. Rao, K.B.S.; Kalluri, S.; Halford, G.R.; McGaw, M.A. Serrated flow and deformation substructure at room temperature in Inconel 718 superalloy during strain controlled fatigue. *Scr. Metal. Mater.* **1995**, *32*, 493–498. [[CrossRef](#)]
32. Praveen, K.V.U.; Sastry, G.V.S.; Singh, V. Room temperature LCF behaviour of superalloy IN718. *Trans. Indian Inst. Met.* **2004**, *57*, 623–630.
33. Zhong, L.Q.; Liang, Y.L.; Yan, Z.; Hu, H. Effect of shot peening on high cycle fatigue limit of FGH4097 P/M superalloys at room temperature. *Rare Metal Mater. Eng.* **2018**, *47*, 2198–2204.
34. Ma, X.; Duna, Z.; Shi, H.; Murai, R.; Yanagisawa, E. Fatigue and fracture behavior of nickel based superalloy Inconel 718 up to the very high cycle regime. *J. Zhejiang Univ. Sci. A* **2010**, *11*, 727–737. [[CrossRef](#)]
35. Xie, X.C.; Cai, Z.G.; Li, Q.; Tang, C.F.; Zhao, Z.Y. Fracture performance of direct aging GH4169 superalloy. *J. Aeronaut. Mater.* **2015**, *35*, 46–56.
36. Merrick, H.F. The low cycle fatigue of three wrought nickel-base alloys. *Metall. Trans.* **1974**, *5*, 891–897. [[CrossRef](#)]
37. Pang, J.C.; Li, S.X.; Wang, Z.G.; Zhang, Z.F. General relation between tensile strength and fatigue strength of metallic materials. *Mater. Sci. Eng. A* **2013**, *564*, 331–341. [[CrossRef](#)]
38. Belan, J. The fractography analysis of IN 718 alloy after fatigue test. *Key Eng. Mater.* **2014**, *635*, 9–12. [[CrossRef](#)]
39. Belan, J. High Frequency Fatigue Test of IN 718 Alloy—microstructure and fractography evaluation. *Metalurgija* **2015**, *1*, 59–62.
40. Yan, N.; Han, X.Q.; Yu, Y.H.; Yu, Y.H.; You, M.; Peng, W.J. Very high cycle fatigue properties of GH4169 Ni-based superalloy. *Mater. Mech. Eng.* **2016**, *40*, 9–12.
41. Wang, Q.Y.; Matsuyama, Y.; Kawagoishi, N.; Goto, M.; Morino, K. Influence of microstructure on fatigue properties of Ni-base superalloy at elevated temperature. In *Fracture of Nano and Engineering Materials and Structures*; Springer: Dordrecht, The Netherlands, 2006; pp. 247–248.
42. Zhang, Y.; Duan, Z.; Shi, H. Comparison of the very high cycle fatigue behaviors of Inconel 718 with different loading frequencies. *Sci. China* **2013**, *56*, 617–623. [[CrossRef](#)]

43. Kawagoishi, N.; Chen, Q.; Nisitani, H. Fatigue strength of Inconel 718 at elevated temperatures. *Fatigue Fract. Eng. Mater. Struct.* **2000**, *23*, 209–216. [[CrossRef](#)]
44. Ayesta, I.; Izquierdo, B.; Flaño, O.; Sánchez, J.A.; Albizuri, J.; Avilés, R. Influence of the WEDM process on the fatigue behavior of Inconel[®] 718. *Int. J. Fatigue* **2016**, *92*, 220–233. [[CrossRef](#)]
45. Ritchie, R. Influence of microstructure on near-threshold fatigue-crack propagation in ultra-high strength steel. *Met. Sci.* **1976**, *11*, 368–381. [[CrossRef](#)]



© 2018 by the authors. Licensee MDPI, Basel, Switzerland. This article is an open access article distributed under the terms and conditions of the Creative Commons Attribution (CC BY) license (<http://creativecommons.org/licenses/by/4.0/>).